Self-assembled Plasmonic Au-TiO₂ Supraparticles for Enhanced Photocatalytic Hydrogen Peroxide Generation

Rajeshreddy Ninakanti*, Rituraj Borah, Karthick Raj AG, Andrea Guidetti, Sabine Van Doorslaer, Radu-George Ciocarlan, Pegie Cool, Kimberley Elbrink, Filip Kiekens, Sara Bals, Sammy W. Verbruggen

R. Ninakanti, R. Borah, K. R. AG, S. W. Verbruggen
Antwerp Engineering, photoelectrochemistry and sensing (A-PECS), Department of Bioscience Engineering, University of Antwerp, Groenenborgerlaan 171, Antwerp, 2020, Belgium
Email:sammy.verbruggen@uantwerpen.be

R. Ninakanti, S. Bals
Electron Microscopy for Material Science (EMAT), Department of Physics, University of Antwerp, Groenenborgerlaan 171, Antwerp, 2020, Belgium

R. Ninakanti, R. Borah, K. R. AG, S. Bals, S. W. Verbruggen
NANOlight Centre of Excellence, University of Antwerp, Antwerp, 2020, Belgium

A. Guidetti, S. V. Doorslaer
Theory and Spectroscopy of Molecules and Materials (TSM²), Department of Chemistry, University of Antwerp, Universiteitsplein 1, Antwerp, 2610, Belgium

R.-G. Ciocarlan, P. Cool
Laboratory for Adsorption and Catalysis (LADCA), Department of Chemistry, Universiteitsplein 1, Antwerp, 2610, Belgium

A. Guidetti, S. V. Doorslaer, R. G. Ciocarlan, P. Cool
CASCH Centre of Excellence, University of Antwerp, Antwerp, 2610, Belgium

K. Elbrink, F Kiekens
Natural Materials & Nutrition Research and Analysis – Pharmaceutical Technology (NatuRAPT), Department of Pharmaceutical Sciences, Universiteitsplein 1, Antwerp, 2610, Belgium

Keywords: self-assembly, supraparticles, plasmonics, photocatalysis, hydrogen peroxide

1

Abstract

Plasmonic nanoparticles deposited on semiconductors have shown great promise in photocatalysis. In the present study, we demonstrate the synthesis of Au-TiO$_2$ supraparticles by self-assembly, leading to collective plasmonic excitation as an effective strategy to enhance the plasmon energy transfer to TiO$_2$. Au-TiO$_2$ supraparticles are synthesized via electrostatic interaction between poly(allylamine hydrochloride)-coated Au nanoparticles and titanium bis(ammonium lactate) dihydroxide (TALH) as the titania precursor. The suprastructure size and density are controlled by varying the amount of TALH in the Au@polymer matrix. The use of large, dense supraparticles (500 nm – 50 µm) enables to double the hydrogen peroxide yield compared to small supraparticles (100 nm – 5 µm). Our mechanistic investigation points at a pivotal role of a strongly increased near-electric field enhancement and associated hot electrons that partake in the reaction. Radical quenching experiments and EPR spectroscopy further confirm the importance of an electron-transfer-based O$_2$-reduction pathway at the root of the enhanced photocatalytic H$_2$O$_2$ production.

1. Introduction

Hydrogen peroxide (H$_2$O$_2$) has been widely used as a clean oxidant in industrial processes, such as organic synthesis,[1] disinfection,[2] water treatment,[3] *etc*. Photocatalysis provides a green way for H$_2$O$_2$ production in contrast to the industrially applied anthraquinone process,[4] since the latter is an energy intensive process that requires large amounts of organic solvents, making it environmentally unfriendly. The primary pathways of photocatalytic H$_2$O$_2$ production include the oxygen reduction reaction (ORR) and the water oxidation reaction (WOR). The photoinduced WOR pathway for H$_2$O$_2$ generation is a two-hole pathway (eq 1). At the same time, competitive reactions of single-hole and four-hole WOR occur that yield hydroxyl radicals ($^\cdot$OH) (eq 2) and O$_2$ (eq 3), respectively.[5, 6] Although the hole-induced $^\cdot$OH can pair together to form H$_2$O$_2$ (eq 4), the high concentration of $^\cdot$OH is a prerequisite, which limits the yield of H$_2$O$_2$.[6] Moreover, the light-driven two-hole WOR path involves a high oxidation potential, and the as-formed H$_2$O$_2$ is easily decomposed (eq 5).[7] Therefore, photocatalytic WOR for H$_2$O$_2$ synthesis is generally not the preferred route. The energy potential (*E*) required to carry out the WOR is given with respect to the normal hydrogen electrode (NHE) at pH 0.[8]

$$2H_2O + 2h^+ \rightarrow H_2O_2 + 2H^+ \qquad E= +1.78\,V \qquad (1)$$

$$H_2O + h^+ \rightarrow {}^\cdot OH + H^+ \qquad E= +2.73\,V \qquad (2)$$

$$2H_2O + 4h^+ \rightarrow O_2 + 4H^+ \qquad E= +1.23\,V \qquad (3)$$

2

$$\cdot OH + \cdot OH \rightarrow H_2O_2 \qquad\qquad\qquad (4)$$

$$H_2O_2 + h^+ \rightarrow O_2^-\cdot + H^+ \qquad\qquad E= +1.00\,V \qquad\qquad (5)$$

Redox reactions associated with the photocatalytic production of H_2O_2 from ORR are summarized below in eq. (6)-(9) with the electrode potentials (E) expressed with respect to the normal hydrogen electrode (NHE) at pH 0.[8]

$$O_2 + e^- \rightarrow O_2^-\cdot \qquad\qquad E = -0.33\,V \qquad\qquad (6)$$

$$O_2^-\cdot + 2H^+ + e^- \rightarrow H_2O_2 \qquad\qquad E = +1.44\,V \qquad\qquad (7)$$

$$O_2 + 2H^+ + 2e^- \rightarrow H_2O_2 \qquad\qquad E = +0.695\,V \qquad\qquad (8)$$

$$O_2 + 2H^+ + 4e^- \rightarrow 2H_2O \qquad\qquad E = +1.23\,V \qquad\qquad (9)$$

$$H_2O_2 + e^- \rightarrow \cdot OH + OH^- \qquad\qquad E = +0.87\,V \qquad\qquad (10)$$

The synthesis of H_2O_2 can be performed through a two-step single-electron ORR route (eq. 6-7) or a one-step two-electron ORR route (eq. 8) through the proton-coupled electron-transfer process, in which the protons are predominantly originating from H_2O or organic electron donors. Due to the presence of a four-electron ORR competing reaction (eq. 9) the selectivity of H_2O_2 formation employing oxygen is often lowered. In addition, because the formation of O_2^- not only requires a more negative potential (−0.33 V) than the one-step two-electron route (0.695 V), and may induce multiple unpredictable reactions, the low efficiency of step (7) also limits the H_2O_2 yield and selectivity. Therefore, the one-step two-electron route is more advantageous. The decomposition of H_2O_2 in reaction (10) cannot be negated entirely, but the one-step two-electron ORR is thermodynamically more favorable. Thus, the key challenge to photocatalytic H_2O_2 synthesis is the development of a catalyst that has both high activity and selectivity for two-electron ORR. In that context, the addition of plasmonic Au nanoparticles to TiO_2 has previously been shown to increase the H_2O_2 production rate via this two-electron ORR.[9] This concept can now be further exploited using hybrid plasmonic structures, as explained below.

Plasmon-enhanced photocatalysis represents a promising avenue due to its potential to harness solar energy more efficiently.[10–12] This technology typically involves the use of plasmonic nanoparticles such as gold (Au) and silver (Ag), coupled with semiconductor materials such as TiO_2 to enhance light absorption and catalytic efficiency.[10] When coupled with plasmonic nanoparticles, TiO_2 can benefit from enhanced light absorption and improved charge carrier generation, separation and utilization, leading to increased photocatalytic efficiency. The localized surface plasmon resonance (LSPR) of these metal nanoparticles results in enhanced electromagnetic fields that can be harnessed to drive photocatalytic reactions.[13], [14] However,

3

despite this progress, the efficiency of plasmon-enhanced photocatalysis is often refrained by the limited extent of interaction between the plasmonic nanoparticles and the semiconductor. Most systems rely on the LSPR of isolated metal nanoparticles, randomly deposited on the semiconductor surface, which constraints the photoconversion efficiency due to limited energy transfer possibilities. The synthesis of composite materials that combine plasmonic nanoparticles with semiconductors more effectively, offers a pathway to overcome these limitations.[11], [12], [15], [16] For instance, a study from some of the co-authors has recently shown the advantage of fully embedding Au NPs in a TiO_2 thin film to increase the area of interaction between the plasmonic particle surface and the semiconductor.[17] Organizing Au nanoparticles into self-assembled, closely arranged structures is also promising to further enhance the photocatalytic activity through plasmonic coupling of closely separated particles in the assembly, a concept that is already commonly exploited in photothermal and sensing applications.[18-21] The challenge thus lies in creating a composite structure where the plasmonic nanoparticles are in close proximity to each other as well as to the semiconductor to enhance the energy-transfer efficiency.

Recent advances in nanotechnology and colloidal synthesis procedures have enabled the synthesis of such closely packed nanostructures, including nano-chains,[19] self-assembled films,[20] and self-assembled supraparticles where nanoparticles form a single three dimensional entity unlike layered films.[21] These structures can potentially provide a more effective platform for plasmon-plasmon and plasmon-semiconductor interactions compared to traditional composites with isolated nanoparticles.[10], [11] For example, Herran et $al.$ prepared a two-dimensional bimetallic catalyst by incorporating platinum nanoparticles into a well-defined super-crystal of gold nanoparticles exhibiting an H_2 evolution rate of 139 mmolg^{-1}h^{-1}.[20] Shi et $al.$ prepared self-assembled Au-CdSe nanocrystal clusters with a 10-fold enhancement in photocatalytic H_2 evolution.[21] Electrostatic self-assembly provides a straightforward and effective method for creating self-assembled structures. Research has demonstrated the versatility and effectiveness of electrostatic self-assembly in a broad range of applications, including photocatalysis. [22], [23] In this study, electrostatic self-assembly aids in maintaining the nanoparticles' stability, with TiO_2 at the surface and without the influence of ligands that could potentially block active sites. This is in strong contrast to surfactant-based self-assembly approaches where ligand coverage may hamper the availability of the active sites and as a result may decrease the photocatalytic activity.[23]

In the current study, the insights that plasmonic Au NPs facilitate H_2O_2 production, and the general concept that supraparticles can boost plasmon-plasmon and plasmon-semiconductor

4

interactions, are combined and leveraged into the integrated solution of Au-TiO$_2$ supraparticles (SPs) as a novel approach to enhance plasmon-enhanced photocatalytic H$_2$O$_2$ generation. The unique aspect of these SPs is their ability to facilitate collective plasmonic excitation, a phenomenon where the plasmonic response of the entire particle assembly is greater than the sum of its individual components.[24], [25] This collective behavior is expected to enhance the plasmonic effects on the semiconductor, leading to more efficient energy transfer and improved photocatalytic performance. The synthesis of these SPs involves a controlled electrostatic interaction between poly(allylamine hydrochloride)-coated Au nanoparticles and titanium ammonium lactate hydroxide (TALH). This process not only allows for the formation of the SPs but also offers a tunable approach to manipulate their size, which is crucial for optimizing their photocatalytic activity. Surface Enhanced Raman Spectroscopy (SERS) and radical trapping experiments involving Electron Paramagnetic Resonance (EPR) Spectroscopy and different probe molecules give an understanding that the enhancement can primarily be attributed to a combination of near-field enhancement and associated hot-electron injection from the Au nanoparticles to TiO$_2$, facilitating the electron-mediated photocatalytic ORR of O$_2$ to H$_2$O$_2$. These results not only demonstrate the potential of Au-TiO$_2$ SPs in plasmon-enhanced photocatalysis but also provide valuable insights into the design of more efficient plasmonic photocatalytic materials.

2. Results and Discussion

2.1. Synthesis

Au nanoparticles of 15 ± 1.8 nm in size were synthesized using a modified Turkevich method. The nanoparticles are monodisperse with a narrow distribution of size and error of ± 1.8 nm with similar results reported previously.[26], [27] The nanoparticles are stabilized by citrate molecules and therefore have a negative zeta potential as mentioned in Figure 1. Next, a thin layer of PAH (1.5 ± 0.3 nm) is coated on the Au nanoparticle surface. Since PAH is a cationic polyelectrolyte, consequently, the zeta potential of the colloidal suspension containing Au@PAH core-shell nanoparticles changes from negative to positive at pH 6. The isoelectric point of PAH is at pH 10.[28] The solutions of Au nanoparticles, PAH and TALH have a pH of 5.5, 5.2 and 6.2, respectively. Therefore, the pH of the suspension was not changed so as to have a net positive surface charge.[29] Subsequently, TALH of varying concentrations was added to the prepared Au@PAH suspension. TALH has a negative zeta potential arising from the lactate and hydroxyl groups. By increasing the amount of TALH injected into the Au@PAH

5

colloid, this ultimately enabled to obtain structures of a) closely arranged small SPs (Au@CloseSmall), b) closely arranged large SPs (Au@CloseLarge), and c) distantly arranged small SPs (Au@DistantSmall) of Au@PAH@TALH. For full clarity, the notation 'small/large' is with respect to the overall supraparticle size, and not the size of the constituting Au nanoparticles, which is fixed at 15 nm. After SP formation, the hybrid structures were subjected to a calcination step at 450°C for 30 mins to convert the TALH precursor into a photocatalytically active crystalline TiO_2 phase.

As schematically represented in Figure 1, as the volume of TALH precursor solution increases, the zeta potential of the suspension at pH 6 changes from positive to approximately zero and eventually to negative. When the zeta potential is positive/negative, the net positive/negative charge results in electrostatic repulsion. It is clear that as the zeta potential changes from positive to zero, the SP size increases from small SP (Figure 2c) and reaches a maximum close to zero as observed in Figure 2d. With further decrease of the zeta potential to negative values, the SP size again decreases (Figure 2e). As the net surface charge decreases, the repulsion is also decreased and results in attractive forces between the negatively charged Au@polymer nanoparticle and positively charged TALH. Therefore, the nanoparticles interact with TALH and start forming SPs. As the zeta potential is close to zero, we consequently observe clustering of nanoparticles, leading to the formation of large SPs. The successful synthesis of these SPs was confirmed by correlating the zeta potential changes with the observed structural evolution, as studied through various electron microscopy techniques. The structural characterization of the synthesized SPs is crucial for understanding the interplay between surface charges and particle assembly, and this relationship is clearly observed in the electron microscopy images discussed below.
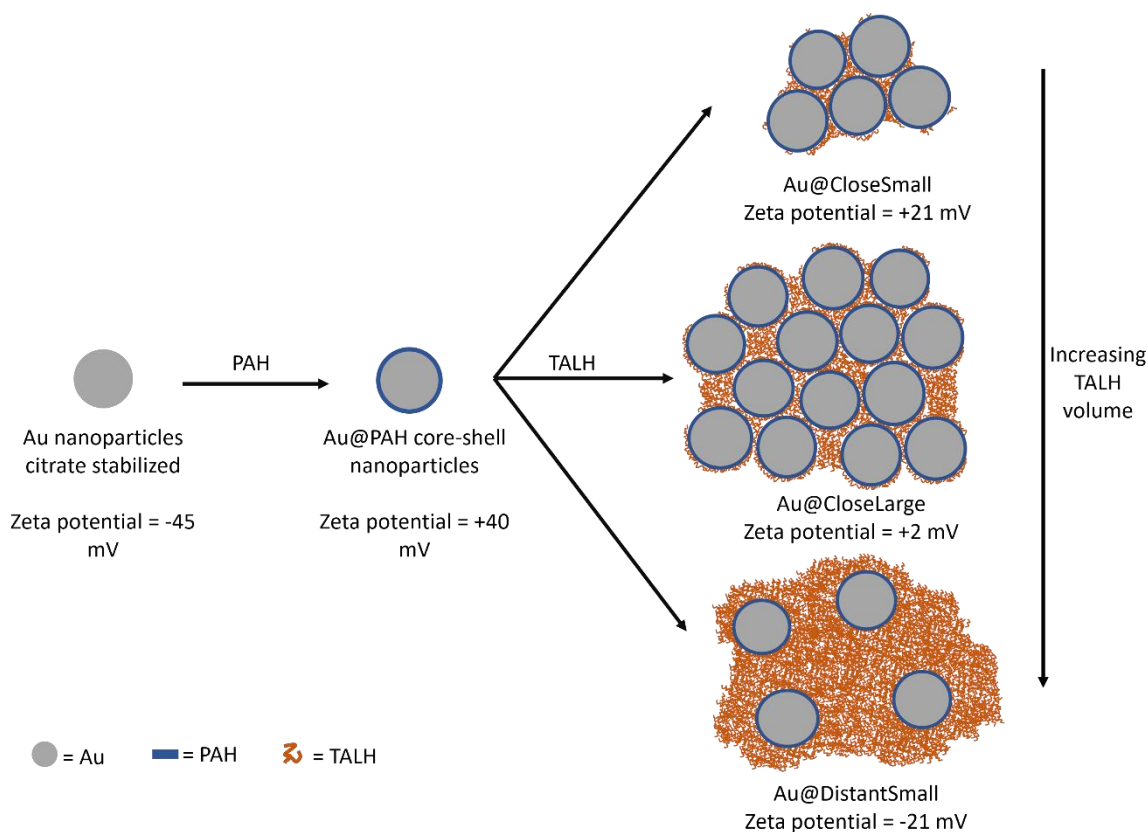
Figure 1. Schematic representation of synthesis of Au-TiO$_2$ supraparticles with varying size as Au@CloseSmall, Au@CloseLarge and Au@DistantSmall

2.2. Structural characterization

The structure of the SPs was studied using bright field transmission electron microscopy (BFTEM), high angle annular dark field scanning transmission electron microscopy (HAADF-STEM) and scanning electron microscopy (SEM). As seen in Figure 2 a-b, the Au nanoparticles have an average size of 15 ± 1.8 nm with a 1.5 ± 0.3 nm shell of PAH for Au@PAH nanoparticles. After mixing the Au@PAH core-shell nanoparticles with TALH, the Au@CloseSmall SPs are formed (Figure 2c) due to net attracting charges with formation of SPs ranging from 100 nm to 500 nm. As the amount of TALH is increased, Au@CloseLarge SPs are formed. As seen in Figure 2d, the Au@CloseLarge SPs can attain dimensions of over a micrometer and do not fit the full field of view of the HAADF-STEM image. Upon adding even higher amounts of TALH, the SP size again decreases to between 100 nm to 500 nm, but due to the high amount of TiO$_2$ precursor, the Au nanoparticles within the SP are arranged more distantly compared to the closely arranged structure of Au@CloseSmall and Au@CloseLarge SPs (Figure 2e). The space between the Au nanoparticles is now filled with a network of TiO$_2$.

7

In order to determine the size of the larger Au@CloseLarge SPs, scanning electron microscopy (SEM) was employed. The SEM image and energy dispersive x-ray (EDX) map in Figure 2 f-i, reveals Au@CloseLarge SPs of 2 μm to 4 μm in size. X-ray diffraction (XRD) pattern (Figure 2j) and selected area electron diffraction (Figure S1) of Au@CloseLarge clearly shows the bands representing crystalline TiO_2 (anatase and rutile phase) and Au with no difference in XRD band reflections observed for Au@CloseSmall and Au@DistantSmall (Figure S2). It can be observed that for all the SPs the size and shape of SPs is non-uniform. This is mainly as kinetics of electrostatic interactions are in general difficult to control. Some studies have attempted to control the kinetics by varying pH and using different solvents, but in that case controlling the directionality to form a structured crystal is not viable.[30]
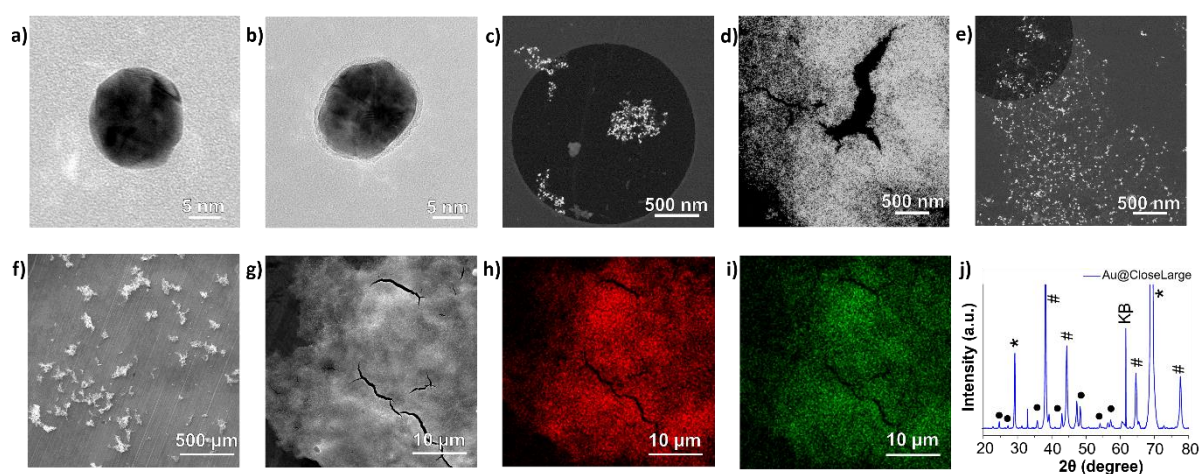
Figure 2. TEM image of a) 15 nm Au nanoparticle and b) Au nanoparticle with PAH shell of 1.5 nm. HAADF-STEM image of c) Au@CloseSmall, d) Au@CloseLarge and, e) Au@DistantSmall. f-g) SEM image of Au@CloseLarge with varying magnification. EDX map of Au@CloseLarge SPs with map of h) Au and i) Ti. j) XRD pattern of Au@CloseLarge with ● representing TiO_2 bands, # representing Au and * representing Si from the Si wafer in the background.

2.3. Optical characterization

2.3.1 UV-Vis and diffused reflectance spectra (DRS)

TALH in itself is not photocatalytically active and is therefore subjected to a calcination step at 450°C for 30 mins to convert it into a photocatalytically active crystalline TiO_2 phase in the SPs (as confirmed by XRD in Figure 2j). The UV-Vis and DRS of all the synthesized materials before and after calcination are represented in Figure 3 a-b. Figure 3a represents the UV-Vis spectra of Au-TiO_2 SP before calcination. It can be observed that the clear plasmon band between 500–550 nm becomes less pronounced, and the absorbance is extended across the

8

entire visible range when moving from Au@CloseSmall to Au@CloseLarge. The extended absorption cross-section of larger Au@CloseLarge SPs is in accordance with previous studies.[31] For the Au@DistantSmall SPs, the plasmon band reemerges. After calcination at 450°C, the DRS spectra are quite similar to those before calcination with minor differences as observed in Figure 3b. One of the main differences is a clearer and more pronounced absorption onset from 380 nm and below, which can be attributed to the bandgap of TiO_2. An extended broadening is observed around 450 nm which can be attributed to the supporting silicon wafer. In these experimental far-field spectra, the closely arranged Au nanoparticles almost behave like a continuous and infinite thin film. The 15 nm Au nanoparticles considered in the current study have low scattering intensity, making the far field coupling very low or negligible.
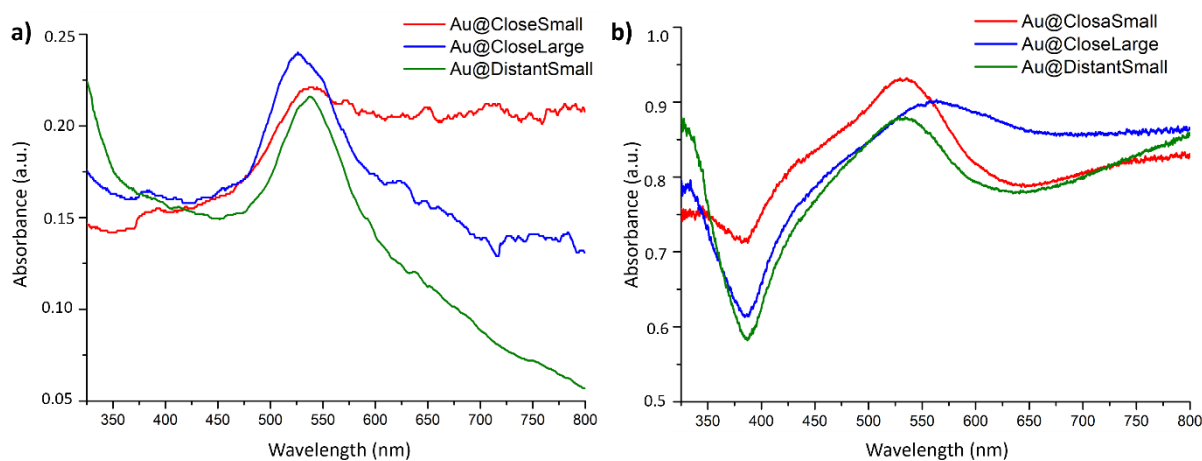

Figure 3. a) UV-Vis spectra of Au-TiO_2 composites in solution before calcination, b) UV-DRS of Au-TiO_2 composites on a silicon wafer after calcination.

2.3.2 Electron energy loss spectroscopy (EELS)

The UV-Vis and DRS spectra demonstrate the far-field effects but do not provide much information about the near-field interactions. Using EELS, more insight is gained into the near-field interactions of Au nanoparticles surrounded by dielectric TiO_2 in the SPs. The EELS spectra obtained adjacent to the surface of Au@CloseLarge display a very pronounced coupling of plasmon bands from closely separated Au nanoparticles as shown in Figure 4. In contrast, the spectra obtained from the core region of the same SP present a single plasmon band, corresponding to that of an isolated Au nanoparticle. This indicates that the plasmon resonance from an array of multilayer Au nanoparticles significantly enhances near-field coupling compared to that from two adjacent Au nanoparticles. The extended absorption observed in the UV-Vis spectra in Figure 3a may thus arise from the coupling of multiple plasmon modes from the SP surface.
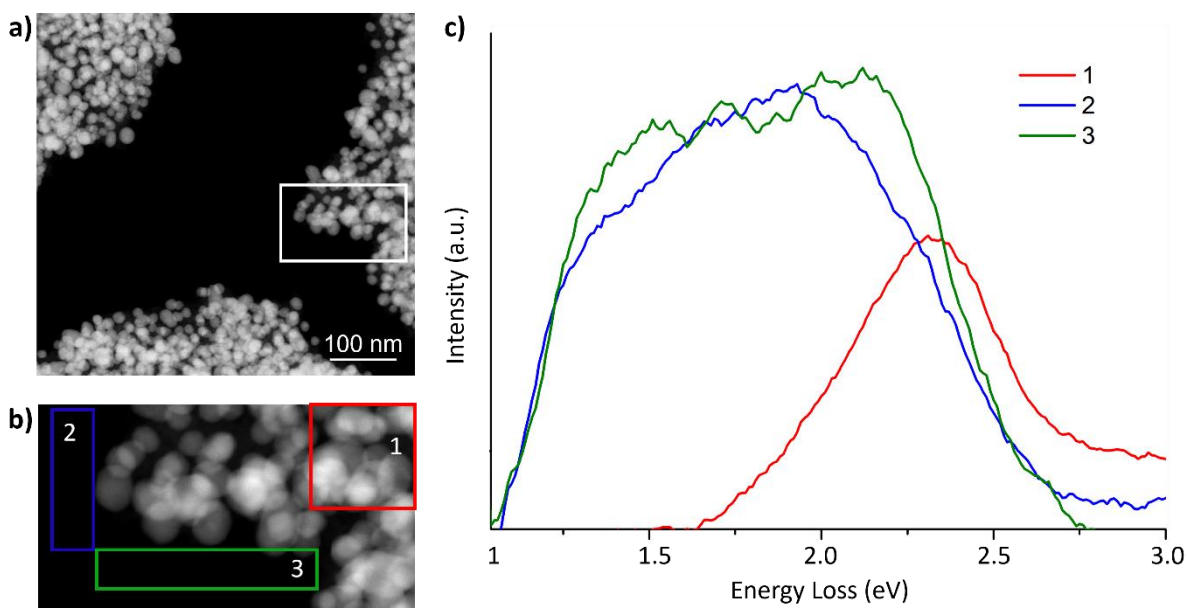
9

Figure 4. a) HAADF-STEM image of Au@CloseLarge, b) inset of HAADF-STEM image in a) used for EELS and, c) EELS spectrum of 3 different selected regions.

2.3.3 Surface enhanced Raman spectroscopy (SERS)

The effect of near-field enhancement with varying sizes of SPs is experimentally substantiated by means of SERS, using Rhodamine 6G as probe molecule on thin films of Au-TiO$_2$ SPs (Figure 5a). Equal amounts of R6G have been deposited on equal weights of nanoparticle films. Notably Au@CloseLarge has a higher enhancement in SERS signal compared to the other SPs, which is in line with expectation based on the EELS data. On the other hand, the weight-based deposition may have an influence on the number of nanoparticles available for Au@DistantSmall. Still, despite being closely spaced, Au@CloseSmall SPs show a lower SERS enhancement compared to Au@CloseLarge, indicating that the plasmonic coupling in larger SPs with closely spaced plasmonic nanoparticles leads to greater near-field enhancement.
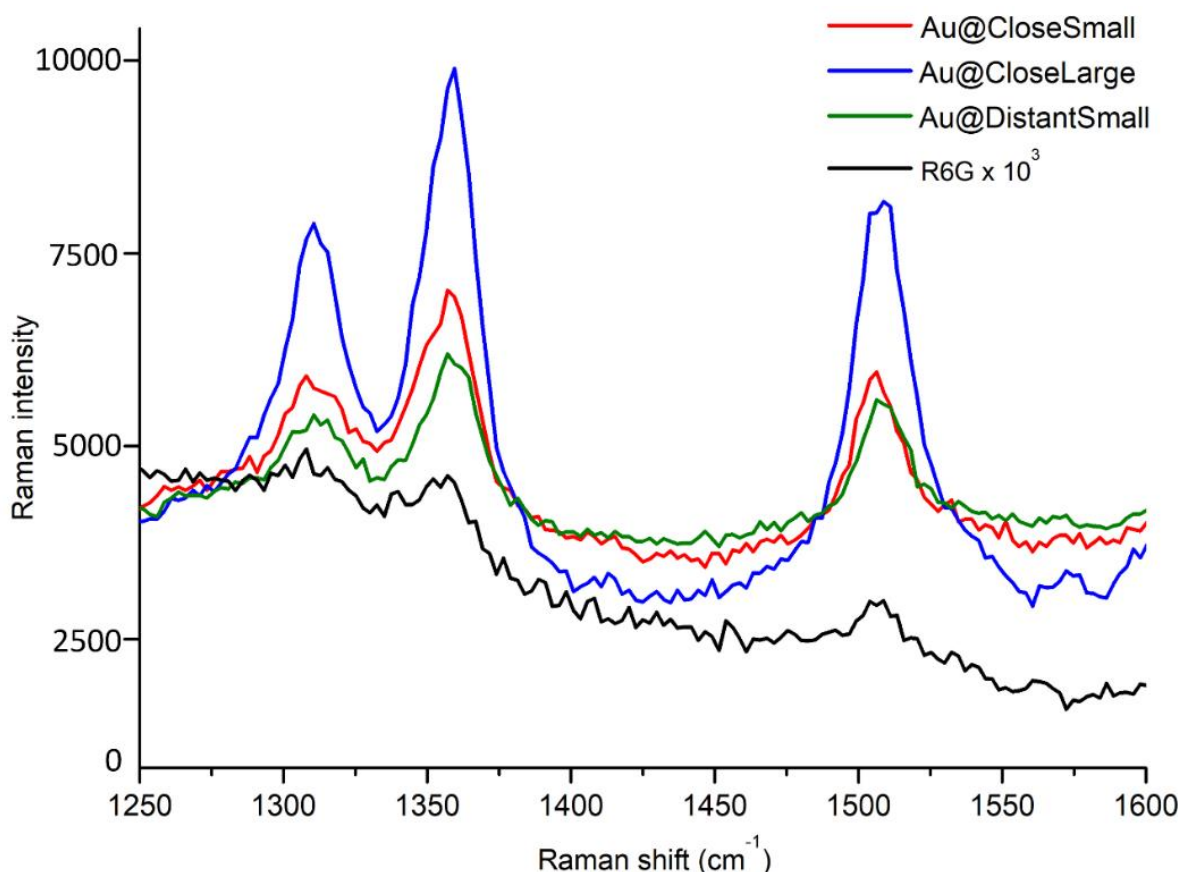
10

Figure 5. Surface enhanced Raman spectra obtained with a 785 nm laser, of Au-TiO$_2$ SPs using R6G as the probe molecule. A higher intensity indicates stronger Raman scattering.

2.4 Photocatalytic generation of hydrogen peroxide

The photocatalytic hydrogen peroxide production of the as-prepared photocatalysts was studied in water and 10% methanol at atmospheric pressure and saturated by oxygen. The reaction conditions were optimized with the temperature kept at 5–8°C using ice and a pH of 4, as established in previous work.[7] Au@CloseLarge show the best activity among the catalysts studied in this work, with a yield of 1.54 mmol h^{-1} m^{-2} using simulated solar light. Pristine TiO$_2$ yields H$_2$O$_2$ at a rate of only 0.22 mmol h^{-1} m^{-2}. Figure 6 clearly shows the effect of the larger SPs on the photocatalytic performance of the composite catalyst, indicating that the use of Au@CloseLarge enhances the catalytic activity under simulated solar light by more than 7 times compared to pristine TiO$_2$, and it is twice that of the smaller Au-TiO$_2$ SPs. To further understand the photocatalytic mechanism of the catalysts, the difference in hydrogen peroxide production rate at wavelengths of 385 nm, 515 nm and simulated solar light was studied. Upon excitation at 385 nm, the TiO$_2$ bandgap can be overcome, the 515 nm source corresponds to the maximal LSPR wavelength, and solar light provides a broadband source that integrates both. The intensities of the light sources for 385 nm, 515 nm and simulated solar light excitation were 5 mW.cm^{-2}, 25 mW.cm^{-2} and 100 mW.cm^{-2}, respectively. Using 385 nm light, TiO$_2$ performs

11

much better than its plasmonic counterpart. Surprisingly, the Au-TiO$_2$ SPs demonstrate much lower H$_2$O$_2$ generation rates upon excitation by light of individual wavelengths of 385 nm and 515 nm, compared to excitation by light of both wavelengths simultaneously, or when using simulated solar light. Moreover, the H$_2$O$_2$ generation using 385 nm and 515 nm wavelength simultaneously is equivalent to the H$_2$O$_2$ generation using simulated solar light. This underlines that simultaneous excitation by UV and visible light at the plasmon resonance frequency is necessary to trigger the synergistic effect of both exciting the plasmonic Au and creating electron-hole pair formation and separation in TiO$_2$. The lower total irradiance when combining the 385 nm and 515 nm light sources, compared to that of simulated solar light, indicates an expected dominant contribution of excitation at the maximum plasmon resonance wavelength, compared to broadband light intensity from simulated solar light.
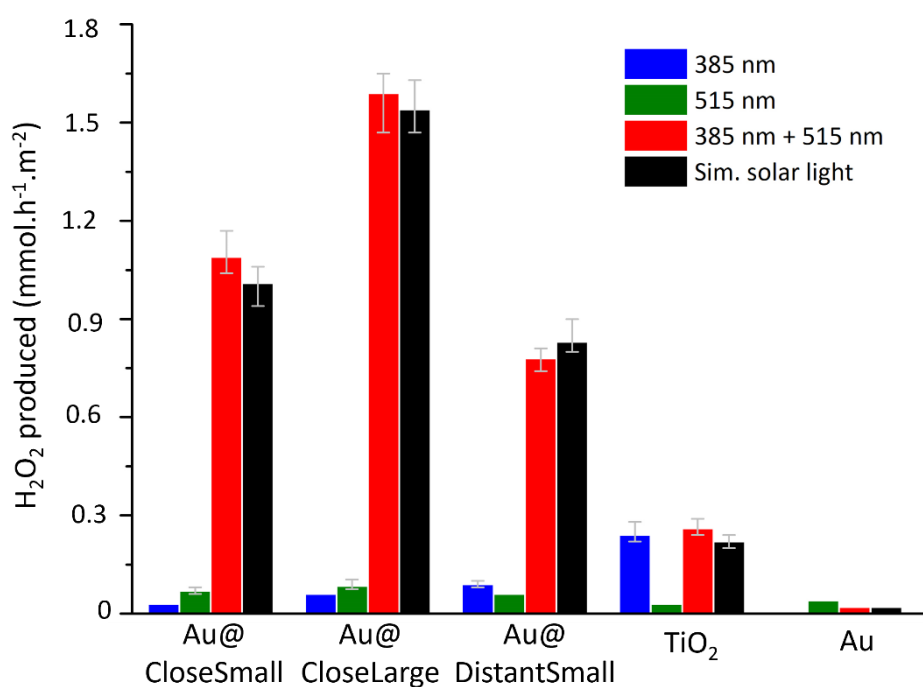

Figure 6. Photocatalytic hydrogen peroxide production of Au, TiO$_2$ and its composites under light illumination of 385 nm, 515 nm, 385+515 nm simultaneously, and simulated solar light.

2.5 Mechanism

To elucidate the mechanism of hydrogen peroxide generation by the synthesized SPs, EPR spectroscopy was performed to detect radicals formed during the reaction. The EPR spectroscopy results revealed clear spectral differences when comparing UV light illumination alone with simultaneous illumination of both UV and visible light. Although this provides

12

evidence of a synergistic effect from the simultaneous illumination, it does not yield detailed mechanistic insights into radical formation. To that end, radical trapping experiments were performed, using probe molecules: 2,3-bis-(2-methoxy-4-nitro-5-sulphenyl)-(2H)-tetrazolium-5-carboxanilide (XTT) and terephthalic acid, which acted as electron and hydroxyl radical scavengers, respectively. These probes provided clearer evidence of the electron-mediated oxygen reduction reaction, leading to increased H_2O_2 production. The detailed analysis of the radical trapping experiments using both techniques is discussed below.

2.5.1 Electron Paramagnetic Resonance Spectroscopy

Since the radicals involved are very short-lived, a spin trap, 5,5-Dimethyl-1-pyrroline N-oxide (DMPO) was used, which reacts with these short-lived radicals to form stable DMPO-radical adducts. EPR spectra were taken from samples that were irradiated *ex situ* in the presence of DMPO in a water-methanol mixture, under conditions similar to those used for photocatalytic H_2O_2 generation (detailed in the experimental section).

As illustrated in Figure 7a, UV irradiation on TiO_2 and Au@CloseSmall presents a 6-line EPR spectrum of a C centered radical,[32] whereas for Au@CloseLarge no signal is observed. The C centered radicals are formed when ·OH radicals or ·OCH_3 radicals are generated in the presence of methanol, that are readily trapped by DMPO.[33] The assignment is confirmed by simulations (Figure S3). With green light alone, no signal was observed for any of the catalysts, indicating negligible radical generation, which is also in line with the catalytic test results. However, when both UV and visible light were used simultaneously, the EPR spectra for Au@CloseSmall SPs showed an additional signal due to the DMPO-adduct of the ·OH radical (signal 2, Figure 7b), whereas an additional triplet signal (signal 3, Figure 7b) was observed for Au@CloseLarge SPs representing oxidation of the spin adduct, often indicated as the DMPO-X adduct.[34] The difference in the spectra under simultaneous illumination can be attributed to several effects. Upon simultaneous illumination by UV and visible light, the observation of ·DMPO-OH can result from the decay of ·DMPO-OOH, in its turn resulting from O_2^- formation, and may provide evidence of the pathway of H_2O_2 formation.[35] Additionally, the observation of DMPO-X can also result from oxidation due to excess of ·OH and other radicals or due to higher H_2O_2 photolysis under simultaneous excitation. Another source of ·OH radicals leading to ·DMPO-OH and DMPO-X upon simultaneous illumination at 385 and 532 nm can be the excess ·OH radicals that did not react with the medium. Alternatively, excess electrons can react back with H_2O_2 to produce H_2O and ·OH.[36] While EPR may not provide a fully detailed picture of the ongoing processes, the fact that ·OH radicals and oxidation of the spin adduct are only observed

13

upon simultaneous excitation of UV and visible light, indicates that a synergistic effect indeed occurs that welcomes a more advanced, detailed investigation that is outside the scope of the present study.
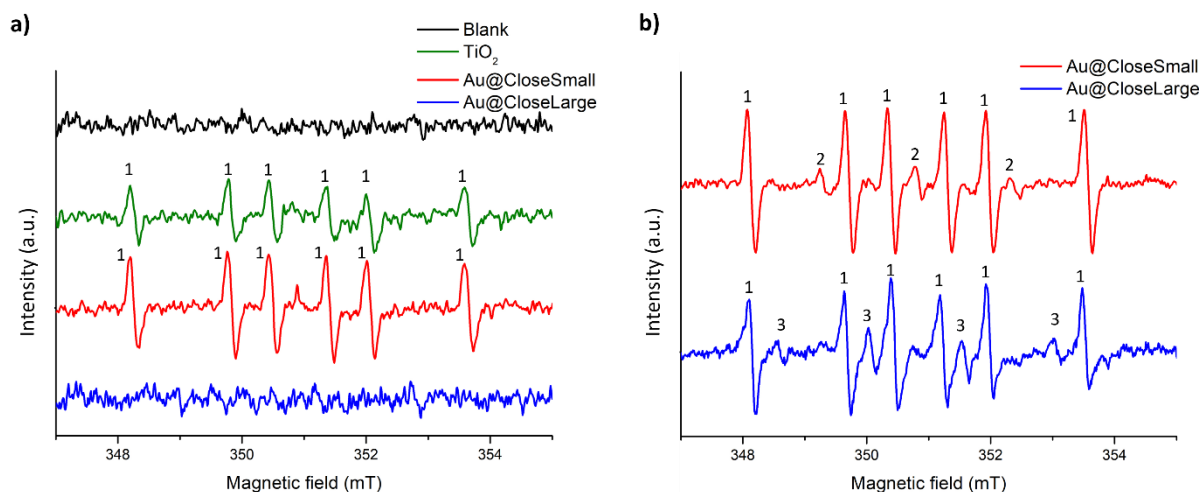

Figure 7. Room-temperature CW-EPR spectra of H_2O:MeOH (3:1) solutions in the presence of the spin trap DMPO (0.01M) of the Au-TiO$_2$ SPs under (a) UV light (385 nm) and (b) UV and green light (385 nm & 532 nm). 1 represents the DMPO-adduct of $CH_2OH\cdot$, 2 represents oxidation of spin adduct and, 3 represents the DMPO-adduct of hydroxyl radical. As a control, the spectra of the UV-illuminated solutions of DMPO and of DMPO with TiO$_2$ are shown.

2.5.2 Radical trapping using XTT and Terephthalic acid as probe molecules

Radical trapping experiments were conducted to better understand the various effects at play. Probe molecules of XTT and terephthalic acid were used as electron scavenger and hydroxyl radical scavenger, respectively, in the presence of excess oxygen and without the interference from methanol. Hydroxyl radicals react with terephthalic acid to produce 2-hydroxyterphthalic acid quantifying the hole-mediated reaction pathway as demonstrated in reference [37]. On the other hand, XTT is reduced by superoxide radicals and an electron to form formazan, and is used to measure the electron-mediated reaction pathway as demonstrated in reference [38]. As observed in Figure 8a and Figure S4a-c, the terephthalic acid probe experiments indicate that the photocatalytic activity of pristine TiO$_2$ relies more strongly on hole-mediated pathways compared to all of the Au-TiO$_2$ SP composites under both solar light and UV light. Under Visible light with 515 nm there was negligible signal for conversion of terephthalic acid, indicating the plasmon response for hole-mediated reactions is not more significant compared to just using TiO$_2$ under UV light. In contrast, as observed in Figure 8b and Figure S4d-f, electron-mediated pathways under solar light irradiation are much more pronounced for Au@CloseLarge compared to TiO$_2$, Au@CloseSmall and Au@DistantSmall, as concluded

14

from the XTT assay. When the light source is changed to just UV light, pristine TiO_2 again dominates the XTT conversion. When using only visible light of 532 nm, there is negligible conversion of XTT.
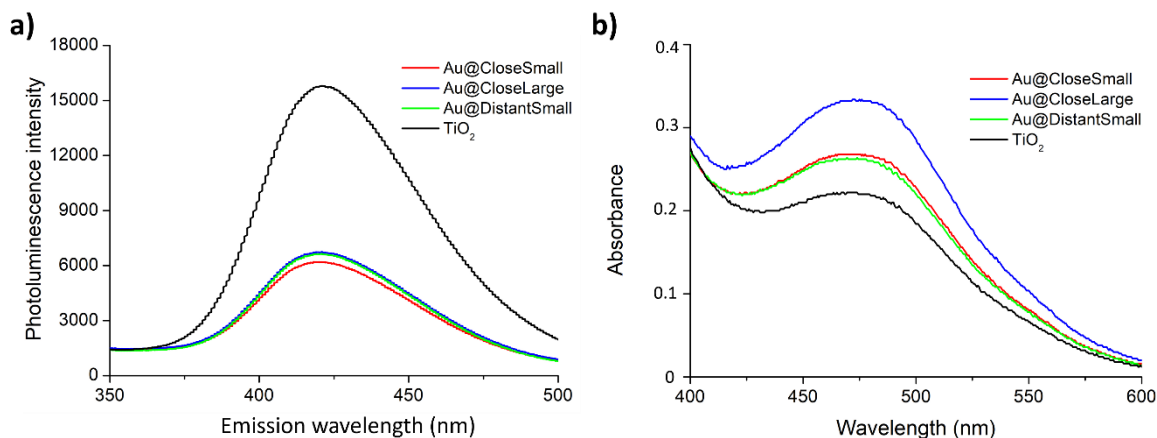

Figure 8. a) Photoluminescence spectra of conversion of terephthalic acid to 2-hydroxyterephthalic acid under simulated solar light illumination on all the Au-TiO2 composites. b) UV-Vis absorption spectra of conversion of XTT to formazan under simulated solar light illumination on all the Au-TiO_2 composites.

The higher contribution of electron and superoxide generation that was probed for Au@CloseLarge under solar light corresponds well with the observed trend in photocatalytic hydrogen peroxide generation. This leads us to an understanding that the H_2O_2 generation on such SPs is occurring mainly through electron-mediated (*i.e.* 2- or 4-electron) O_2 reduction pathways. This is well in line with former studies that have indicated H_2O_2 generation using Au-TiO_2 composites occurs mainly through 2-electron reduction of O_2.[9], [39], [40]

Combining all previous information, we hypothesize that the generation of hot electrons upon plasmonic excitation of the SP is a crucial factor for explaining the superior performance of these materials. Hot electrons are generated at the Au metal sites and are subsequently transferred to the TiO_2 conduction band, leading to an increase in the hydrogen-peroxide generation rate through electron-mediated ORR. For Au@CloseLarge SPs, the generation and transfer of hot electrons from Au to TiO_2 are enhanced because of 1) the close packing of Au nanoparticles, which increases the near-electric field through plasmonic coupling (as shown in the SERS experiments), intensifying hot electron generation, and 2) the packing of Au nanoparticles into a single assembly, which promotes charge separation and charge transfer into the TiO_2 conduction band due to the overflow of electrons from multiple Au nanoparticles. For Au@CloseLarge SPs, the photocatalytic hydrogen peroxide from electron-based reactions

15

could be enhanced because: 1) the close packing of Au nanoparticles can lead to collective lattice resonances which increases the near-electric field through plasmonic coupling, correlating it to a more efficient hot electron generation,[41], [42] 2) the packing of Au nanoparticles into a single assembly, has shown to promote plasmon enhanced resonant energy transfer (PIRET), albeit in Au-CdSe self-assembly of 100 nm in size and micrometer sized Au-CuS nanochains, which can corelate similarly to promote charge separation and charge transfer into the TiO_2 conduction band,[21], [43] and 3) the packing of Au nanoparticles into a single assembly of TiO_2 in multiple layers can promote the dark plasmon modes and therefore hot electron injection through Landau damping.[44]

We further argue that the generation of hot electrons is the pivotal plasmonic mechanism for the present system, as other plasmonic effects are less likely to occur under the present set of experimental conditions. Indeed, the size of Au nanoparticles used in this work (15 nm) implies that scattering of light is not a significant factor, as it only becomes important for nanoparticles largely exceeding 50 nm. Additionally, plasmonic local thermal heating within the Au composites is expected to be minimal, given the light intensity used is only (at most) 100 mW cm^{-2}, while it has been shown that for photothermal effects to occur, much higher irradiance levels are required.[14] Furthermore, the optical absorption band of TiO_2 and the LSPR band of Au do not align, hence the direct effect of increased charge carrier generation at the semiconductor boosted by the enhanced near-field is hampered. It should be noted that these hypotheses remain theoretical and we would recommend this to be the subject of follow-up experimental studies using time-resolved transient absorption spectroscopy to understand electron transfer dynamics,[45] as well as theoretical investigations using density functional theory to validate the electron transfer dynamics and detect the source of enhanced electron generation.[46]

3. Conclusion

Our findings indicate a significant enhancement in the photocatalytic production of hydrogen peroxide when using Au NPs and TiO_2 self-assembled into supraparticles. The enhancement in the H_2O_2 yield was found to increase with an increase in the supraparticle size. The supraparticle size could be conveniently controlled through the ratio of TiO_2 precursor and PAH-covered Au NPs, by regulating their electrostatic interaction and as such facilitate their self-assembly into micron-sized aggregates. Using SERS and EELS it was shown that the near-field enhancement increases the local electromagnetic field between Au nanoparticles and around the TiO_2, thus

16

drastically improving light absorption through plasmonic coupling within the supraparticles. In addition, EPR spectroscopy and radical quenching experiments were conducted, indicating that under conditions of simultaneous excitation by UV and visible light at the plasmon resonance frequency, the enhanced photocatalytic activity is dominated by electron-mediated reactions, confirming the role of electron-mediated oxygen reduction pathways as major route towards improved photocatalytic H_2O_2 production in the present system. These results not only demonstrate the potential of Au-TiO$_2$ supraparticles in plasmon-enhanced photocatalytic H_2O_2 production, but also provide valuable insights into the design of more efficient plasmonic photocatalytic materials in general.

4. Experimental section

4.1 Synthesis

4.1.1 Au@PAH core-shell nanoparticle synthesis

Gold nanoparticles were synthesized using a modified Turkevich method, as outlined in prior research.[26], [27] In brief, a suitable amount of $HAuCl_4$ was dissolved in a round-bottom flask containing a total of 100 mL of water and brought to a boil. Upon reaching boiling, 1 mL of a 1 wt% sodium citrate solution was added, and the mixture was allowed to boil under vigorous stirring for 30 minutes. After this period, the solution was rapidly cooled to room temperature in an ice bath to halt the reaction. The nanoparticles were then collected by centrifugation at 12,000 rpm and redispersed in water.

To prepare stock solutions of the polyelectrolyte polyallylamine hydrochloride (PAH, MW 17.5 kDa, Sigma-Aldrich), PAH was dissolved in ultrapure water and sonicated for 30 minutes. For further processing, 12 mL of the synthesized colloidal solution was centrifuged at 4,700 g for 40 minutes and redispersed in water, which removed most of the excess citrate. This step minimized the charge interference from citrate molecules, facilitating optimal deposition of the initial polycation layer (PAH). Subsequently, 12 mL of the centrifuged silver colloidal solution was added dropwise to 6 mL of a 5 g/L PAH solution under vigorous stirring in a glass vial. Stirring continued at room temperature for 20 minutes in the dark. The mixture was then centrifuged in 1.5 mL Eppendorf tubes to eliminate excess polyelectrolyte. Approximately 1.46 – 1.48 mL of the supernatant was discarded, and the remaining dark-brown pellet was redispersed in ultrapure water. This centrifugation and redispersion process was repeated as a washing step, yielding a final 12 mL colloidal solution.

4.1.2 Au-TiO$_2$ supraparticle synthesis

The synthesized Au@PAH core-shell nanoparticle colloid is further diluted to 15 mL and 1mL of 10 mM titanium bis(ammonium lactato) dihydroxide (TALH) was added in 100 µL steps. After each 100 L step a zeta potential measurement is taken. Depending on the size of supraparticle to be achieved, the reaction can be stopped when zeta potential reaches +20, around 0 or -20 to obtain Au@CloseSmall, Au@CloseLarge or Au@DistantSmall supraparticles.

4.2 Photocatalytic Hydrogen Peroxide generation

Au-TiO$_2$ SPs were drop casted on a precleaned silicon wafer (3 cm $\times$ 6 cm) and calcined to 450 °C for 2 hours. This led to an approximate photocatalyst loading of 75 µg cm^{-2}. Photometric measurements were performed to determine the gold mass concentration per unit volume in the colloids by appropriate dilution to detection limits using the Spectroquant® gold test kit. The coated silicon wafer was kept in a petri dish surrounded by ice and 27 mL milli-Q water with 3 mL methanol (10%) was added to it. The pH of the reaction solution was adjusted using 10mM nitric acid. Suitable light was illuminated onto the sample to produce H$_2$O$_2$. For simulated sunlight AM1.5G filter was used (SciSun-300, Sciencetech) and the intensity amounted to 100 mW.cm^{-2} (*i.e.* 1 sun) at the top surface of the silicon wafer. LED light sources were used to illuminate using UV (385 nm) and green light (515 nm). The intensity of UV and green light was kept at 5 mWcm^{-2} and 25 mWcm^{-2} respectively. As a reference, hydrogen peroxide generation reaction on blank silicon wafer was performed to omit effects of direct photolysis and heat from light irradiation. Incident light intensity was measured by a calibrated spectroradiometer (Avantes Avaspec-3648-USB2). Hydrogen peroxide measurement was carried out using the KMnO$_4$ titration method.[47]

4.3 Characterization

4.3.1 Electron microscopy

Nanoparticle solution (3 µL) was drop-cast on a Mo grid with a single layer graphene and left to dry in ambient air. High-angle annular dark field scanning transmission electron microscopy (HAADF-STEM) and energy dispersive X-ray spectroscopy (EDS) was performed using a Thermo Fischer Tecnai Osiris microscope operated at 200 kV.

Scanning electron microscopy (SEM) images of the films were acquired using an FEG-ESEM-EDX, Thermo Fisher Scientific Quanta 250 at an accelerating voltage of 20 kV.

4.3.2 Electron energy loss spectroscopy

EELS measurements were carried out using an aberration corrected ThermoFischer Scientific – Titan Cubed electron microscope, operating at 300 kV, equipped with an energy monochromator excited to a value of 0.7. The energy resolution provided by the electron

18

monochromator, as measured from the full-width half maximum of acquired zero-loss peaks, was 100 meV. The dispersion of the spectrometer was set to 0.002 eVch^{-1} to visualize the plasmon edges. To analyze the EELS data sets, EELSModel software was used.[48]

4.3.3 Zeta potential

Zeta potential measurements were carried out on a Zetasizer Nano ZS (Malvern, United Kingdom). The samples were diluted with ultrapure water and measured in triplicate at a temperature of 25 °C. 100 µL of solution was inserted using a syringe into a capillary cuvette with positive and negative potential at each end to measure the zeta potential.

4.3.4 UV-Vis absorption and UV- Vis DRS

A UV–vis absorption spectrum and UV-Vis diffused reflectance spectrum was recorded from 300 nm to 800 nm with a resolution of 0.2nm using Shimadzu UV–vis 2501 PC double beam spectrophotometer. UV–vis absorption spectrum was recorded using liquid sample holder and UV-Vis DRS was recorded by pressing the powdered sample on Barium Sulfate background.

4.3.4 Surface enhanced Raman spectroscopy

Rhodamine 6G (Sigma Aldrich, Fluorescence bioreagent) dye was used as the Raman probe molecule for SERS measurements and all the measurements were done using the same sample and substrate as used for hydrogen evolution reaction and stearic acid degradation tests after clearing off all the organic matter. These substrates were prepared for SERS measurements by drop casting a mixture of known concentration of R6G, 10^{-4} M (20 µL) on the Au@TiO2 core shell thin films. Reference neat R6G Raman substrate is prepared by dropcasting 50 µL of 1M pure R6G dye solution. All the samples were allowed to dry in a desiccator for one full day before measurement. The Raman spectra were recorded on a Horiba XploRA Plus Raman spectrometer equipped with a diode-pumped solid-state laser of 785 nm and a power of 25 mW. The samples were measured with an acquisition time of 10 s, 10 accumulations and in a spectral range of 100–2000 cm^{-1}. Raman spectra were recorded multiple times at different locations for each sample. Fluorescence was observed using 532 nm laser and therefore a laser of 785 nm wavelength was used.

4.3.5 Terephthalic acid and XTT radical trapping experiments

All measurements were done using the same sample and substrate as used for hydrogen evolution reaction and stearic acid degradation tests. For hydroxyl radical trapping experiments, the thin film was inserted in 20 mL of TA (0.5 mM) and NaOH (2 mM) and illuminated with simulated solar light (100 mWcm^{-2}). The fluorescent emission intensity of 2-hydroxyterephthalic acid was detected with λ_{max} at 425 nm under the excitation at 315 nm using a Shimadzu RF-6000 spectrofluorometer, equipped with a Xe lamp. For both excitation and

19

emission, the slit width was set to 2 nm. Fur superoxide radical trapping experiments, the thin film was inserted in 10 mL of XTT sodium salt solution (0.1 mM) in DMSO in a glass vessel and illuminated with simulated solar light (100 mW.cm^{-2}). The resulting supernatant was analyzed using UV-VIS for the formation of XTT formazan with λ_{max} at 475 nm.

4.3.6 Electron paramagnetic resonance spectroscopy

Room-temperature continuous-wave (cw) X-band EPR measurements were carried out on a Bruker Elexsys E680 spectrometer mounted with an optically accessible ER4104OR resonator working at ~ 9.83 GHz. The spectra were collected at 5 mW microwave power, 0.05 mT modulation amplitude, and 100 kHz modulation frequency. DMPO (5,5-dimethyl-1-pyrroline N-oxide) was used to trap any short-lived radicals generated during a photoreaction. The resulting DMPO adduct generally have longer lifetimes allowing for detection by EPR spectroscopy. Here, DMPO was added to water with 25% methanol mixture and EPR spectra were recorded before and after *ex situ* illumination with UV and green light under air atmosphere. The average time to transfer the sample to a glass tube (capillary), centrifuge it and load it into the EPR instrument is approximately 5 minutes. Further details on the illumination and sample preparation are given in the supplementary material.

Author contributions
R.N. – Conceptualization (lead)**,** Formal Analysis, Investigation (lead)**,** Methodology**,** Validation**,** Visualization**,** Writing – Original Draft Preparation (lead)**,** Writing – Review & Editing. **R.B.** – Conceptualization, Investigation, Validation, Writing – Review & Editing. **K.R.A** – Investigation, Validation, Writing – Review & Editing **A.G.** – Formal Analysis, Investigation, Validation, Writing – Review & Editing **S.V.D.** – Resources, Supervision, Writing – Review & Editing **R.G.C.** – Investigation, Validation **P.C.** – Resources, Supervision, Writing – Review & Editing **K.E.** – Investigation, Validation **P.K.** – Resources, Supervision, Writing – Review & Editing **S.B.** – Conceptualization, Funding Acquisition, Resources, Supervision, Writing – Review & Editing **S.W.V** – Conceptualization, Funding Acquisition, Resources, Supervision, Writing – Review & Editing

Data availability statement
The data that support the findings of this study are openly available in Zenodo at http://doi.org/10.5281/zenodo.14050918.[49]

References

[1]   E. T. Poursaitidis, P. L. Gkizis, I. Triandafillidi, C. G. Kokotos, *Chem. Sci.*, **2024**, 15, 1177.

[2]   A. G. Ríos-Castillo, F. González-Rivas, J. J. Rodríguez-Jerez, *J. Food Sci.*, **2017**, 82, 2351.

[3]   R. Guan, X. Yuan, Z. Wu, L. Jiang, Y. Li, G. Zeng, *Chem. Eng. J.*, **2018**, 339, 519.

[4]   J. M. Campos-Martin, G. Blanco-Brieva, J. L. G. Fierro, *Angew. Chemie Int. Ed.*, **2006**, 45, 6962.

[5]   Y. Sun, L. Han, P. Strasser, *Chem. Soc. Rev.*, **2020**, 49, 6605.

[6]   L. Chen, L. Wang, Y. Wan, Y. Zhang, Z. Qi, X. Wu, H. Xu, *Adv. Mater.*, **2020**, 32, 1904433.

[7]   H. Hou, X. Zeng, X. Zhang, *Angew. Chemie Int. Ed.*, **2020**, 59, 17356.

[8]   T. Freese, J. T. Meijer, B. L. Feringa, S. B. Beil, *Nat. Catal.*, **2023**, vol. 6, 553.

[9]   H. Tada, M. Teranishi, S. Naya, *J. Phys. Chem. C*, **2023**, 127, 5199.

[10]   U. Aslam, V. G. Rao, S. Chavez, S. Linic, *Nat. Catal.*, **2018**, 1, 656.

[11]   R. Ninakanti, F. Dingenen, R. Borah, H. Peeters, S. W. Verbruggen, *Top. Curr. Chem.*, **2022**, 380, 40.

[12]   S. Ezendam, M. Herran, L. Nan, C. Gruber, Y. Kang, F. Gröbmeyer, R. Lin, J. Gargiulo, A. Sousa-Castillo, E. Cortés, *ACS Energy Lett.*, **2022**, 7, 778.

[13]   X. Yang, D. Su, X. Yu, P. Zeng, H. Liang, G. Zhang, B. Song, S. Jiang, Small, **2023**, 19, 2205659.

[14]   R. Borah, S. W. Verbruggen, *J. Phys. Chem. C*, **2019**, 123, 30594.

[15]   K. Yang, X. Yao, B. Liu, B. Ren, *Adv. Mater.*, **2021**, 33, 2007988.

[16]   W. Guo, Y. Liu, Y. Sun, Y. Wang, W. Qin, B. Zhao, Z. Liang, L. Jiang, *Adv. Funct. Mater.*, **2021**, 31, 2100768

[17]   H.Peeters, M. Keulemans, G. Nuyts, F. Vanmeert, C. Li, M. Minjauw, C. Detavernier, S. Bals, S. Lenaerts, S.W. Verbruggen., *Appl. Catal. B Enviro*, **2020**, 267, 118654.

[18]   R. Borah, J. Smets, R. Ninakanti, M. L. Tietze, R. Ameloot, D. N. Chigrin, S.Bals, S. Lenaerts, S. W. Verbruggen, *ACS Appl. Nano Mater*, **2022**, 5, 11494.

[19]   G. Yu, J. Qian, P. Zhang, B. Zhang, W. Zhang, W. Yan, G. Liu, **2019**, *Nat. Commun*, 10, 4912.

[20]   M. Herran, S. Juergensen, M.Kessens, D. Hoeing, A. Köppen, A. S.Castillo, W. J. Parak, H. Lange, S. Reich, F. Schulz, E. Cortés, *Nat. Catal.*, **2023**, 6, 1205.

[21] R. Shi, Y. Cao, Y. Bao, Y. Zhao, G. I. Waterhouse, Z. Fang, L. Z. Wu, C.H. Tung, Y. Yin, T. Zhang, *Adv. Mater.*, **2017**, 29, 1700803.

[22] G. O. Bonin, S. J. Barrow, T. U. Connell, A. Roberts, A. S. R. Chesman, D. E. Gómez, *J. Phys. Chem. Lett.*, **2020**, 11, 8378.

[23] S. Lee, K. Sim, S. Y. Moon, J. Choi, Y. Jeon, J. M. Nam, S. J. Park, *Adv. Mater.*, **2021**, 33, 2007668.

[24] D. Liu, C. Xue, *Adv. Mater.*, **2021**, 33, 2005738.

[25] S. G. Park, X. Xiao, J. Min, C. W. Mun, H. S. Jung, V. Giannini, R. Weissleder, S. A. Maier, H. Im, D. H. Kim, *Adv. Funct. Mater.*, **2019**, 29, 1904257.

[26] R. Asapu, N. Claes, R. G. Ciocarlan, M. Minjauw, C. Detavernier, P. Cool, S. Bals S. W.Verbruggen, *ACS Appl. Nano Mater.*, **2019**, 2, 4067.

[27] S. W. Verbruggen, M. Keulemans, M. Filippousi, D. Flahaut, G. V. Tendeloo, S. Lacombe, J. A. Martens, S. Lenaerts, *Appl. Catal. B Environ.*, **2014**, 156–157, 116.

[28] A. Michna, *Adv. Colloid Interface Sci.*, **2017**, 250, 95.

[29] N. Kallay, D. Kovačević, S. Žalac, *Surface Complexation Modelling*, Ed. Elsevier **2006**.

[30] A. Klinkova, R. M. Choueiri, E. Kumacheva, *Chem. Soc. Rev.*, **2014**, 43, 3976.

[31] R. Verma, R. Belgamwar, P. Chatterjee, R. Bericat-Vadell, J. Sa, V. Polshettiwar, *ACS Nano*, **2023**, 17, 4526.

[32] A. Alberti and D. Macciantelli, *Electron Paramagnetic Resonance*, Wiley, Hoboken, NJ **2009**.

[33] K. Makino, T. Hagiwara, A. Hagi, M. Nishi, A. Murakami, *Biochem. Biophys. Res. Commun.*, **1990**, 172, 1073.

[34] L. Chen, S. Kutsuna, S. Yamane, J. Mizukado, *Polym. Degrad. Stab.*, **2017**, 139, 89.

[35] E. Finkelstein, G. M. Rosen, E. J. Rauckman, *Arch. Biochem. Biophys.*, **1980**, 200,1.

[36] L. Zhou, J. Lei, F. Wang, L. Wang, M. R. Hoffmann, Y. Liu, S. I. In, J. Zhang, **2021**, *Appl. Catal. B Environ.*, 288,119993.

[37] T. Zorlu, I. B. Becerril-Castro, A. Sousa-Castillo, B. Puértolas, L. V. Besteiro, Z. Wang, A. Govorov, M. A. Correa-Duarte, R. A. Alvarez-Puebla, *Adv. Funct. Mater.*, **2024**, 2410352.

[38] L. Wang, J. Zhang, Y. Zhang, H. Yu, Y. Qu, J. Yu, *Small*, **2022**, 18, 2104561.

[39] H. Zhou, B. Li, J. Liu, W. Yang, W. Wang, X. Hu, S. Wang, *Process Saf. Environ. Prot.*, **2024,** 183, 355.

[40] G. Zuo, S. Liu, L. Wang, H. Song, P. Zong, W. Hou, B. Li, Z. Guo, X. Meng, Y. Du, T. Wang, V. A. L Roy *Catal. Commun.*, **2019**, 123, 69.

22

[41]   F. Binkowski, T. Wu, P. Lalanne, S. Burger, A. O. Govorov, *ACS Photonics*, **2021**, 8, 1243.

[42]   D. Bosomtwi, M. Osiński, V. E. Babicheva, *Opt. Mater. Express*, **2021**, 11, 3232.

[43]   J. Ma, X. Liu, R. Wang, F. Zhang, G. Tu, *Nano Res.*, **2022**, 15, 5671.

[44]   D. Hoeing, F. Schulz, N. S. Mueller, S. Reich, H. Lange, *J. Chem. Phys.*, **2020**, 152, 64710.

[45]   B. Ostovar, S. A. Lee, A. Mehmood, K. Farrell, E. K. Searles, B. Bourgeois, W. Y. Chiang, A. Misiura,N. Gross, A. Al-Zubeidi, J. A. Dionne, C. F. Landes, M. Zanni, B. G. Levine, S. Link, *Science Advances*, **2024**, 10, p.eadp3353.

[46]   C. J. Herring, M. M. Montemore, *ACS Nanosci. Au*, **2023**, 3, 269.

[47]   N. V Klassen, D. Marchington, H. C. E. McGowan, *Anal. Chem.*, **1994**, 66, 2921.

[48]   J. Verbeeck, S. Van Aert, *Ultramicroscopy*, **2004**, 101, 207.

[49]   R. Ninakanti, R. Borah, K. R. AG, A. Guidetti, S. V. Doorslaer, R. G. Ciocarlan, P. Cool, K. Elbrink, F. Kiekens, S. Bals, S. W. Verbruggen; 2024; Self-assembled plasmonic Au-TiO$_2$ supraparticles for enhanced photocatalytic hydrogen peroxide generation; Zenodo; DOI: 10.5281/zenodo.14050918.

ToC text

Au nanoparticles are electrostatically self-assembled into Au-TiO$_2$ supraparticles by coating Au with a negatively charged polymer and the polymer interacting with positively charged Ti precursor. The self-assembly allows for plasmonic coupling and yields highly efficient H$_2$O$_2$ generation in the presence of O$_2$ and H$_2$O under simulated solar light illumination.

ToC figure